

Alkyl-Substituted Selenium-Bridged V-Shaped Organic Semiconductors Exhibiting High Hole Mobility and Unusual Aggregation Behavior

Toshihiro Okamoto*,^{1,2,3}, Masato Mitani¹, Craig P. Yu¹, Chikahiko Mitsui¹, Masakazu Yamagishi⁴, Hiroyuki Ishii⁵, Go Watanabe⁶, Shohei Kumagai¹, Daisuke Hashizume⁷, Shota Tanaka⁸, Masafumi Yano⁸, Tomokatsu Kushida¹, Hiroyasu Sato⁹, Kuniyoshi Sugimoto^{10,11}, Takashi Kato¹², and Jun Takeya^{1,2,13}

¹Material Innovation Research Center (MIRC) and Department of Advanced Materials Science, School of Frontier Sciences, The University of Tokyo, 5-1-5 Kashiwanoha, Kashiwa, Chiba 277-8561, Japan.

²National Institute of Advanced Industrial Science and Technology (AIST)-University of Tokyo Advanced Operando-Measurement Technology Open Innovation Laboratory (OPERANDO-OIL), AIST, 5-1-5 Kashiwanoha, Kashiwa, Chiba 277-8561, Japan. ³PRESTO, JST, 4-1-8 Honcho, Kawaguchi, Saitama 332-0012, Japan. ⁴National Institute of Technology, Toyama College, 13 Hongo-machi, Toyama, Toyama 939-8630, Japan. ⁵Department of Applied Physics, Faculty of Pure and Applied Sciences, University of Tsukuba, 1-1-1 Tennodai, Tsukuba, Ibaraki 305-8573, Japan. ⁶Department of Physics, School of Science, Kitasato University, 1-15-1 Kitasato, Minami-ku, Sagami-hara, Kanagawa 252-0373, Japan. ⁷RIKEN Center for Emergent Matter Science (CEMS), 2-1 Hirosawa, Wako, Saitama 351-0198, Japan. ⁸Chemistry, Materials and Bioengineering Major, Graduate School of Science and Engineering, Kansai University, 3-3-35 Yamate-cho, Suita, Osaka 564-8680, Japan. ⁹Rigaku Corp., 3-9-12 Matsubara-cho, Akishima, Tokyo 196-8666, Japan. ¹⁰Diffraction & Scattering Division, Japan Synchrotron Radiation Research Institute, 1-1-1 Kouto, Sayo-cho, Sayo-gun, Hyogo 679-5198, Japan.

¹¹Institute for Integrated Cell-Material Sciences (iCeMS), Kyoto University, Yoshida-Honmachi, Sakyo-ku, Kyoto 606-8501, Japan. ¹²Department of Chemistry and Biotechnology, School of Engineering, The University of Tokyo, 7-3-1 Hongo, Bunkyo-ku, Tokyo 113-8656, Japan. ¹³International Center for Materials Nanoarchitectonics (MANA), National Institute for Materials Science (NIMS), 1-1 Namiki, Tsukuba 205-0044, Japan.

Contents

1. Synthesis and Characterization
2. Thermal Analyses: Thermogravimetric Analyses (TGA)
3. Ionization Potentials
4. Single-Crystal Analyses
5. Differential Scanning Calorimetric (DSC) Analyses
6. Powder X-ray Analyses
7. Powder UV-vis Absorption Spectra
8. Time-Dependent Absorption Spectra in Solution and Deposited Thin Film
9. Theoretical Calculations
10. X-ray Diffraction Measurements and AFM Observation for Polycrystalline Films
11. OFET Device Fabrication and Evaluation Procedure
12. References

1. Materials and General for Synthesis and Characterization

Materials

Reagents and Starting Materials: 2,7-Dibromonaphthalene, trimethylsilyl chloride, 2,2,6,6-tetramethylpiperidine (TMP), isopropylmagnesium bromide (*i*-PrMgBr), and tetrakis(triphenylphosphine)palladium(0) were purchased from TCI. TMP was distilled prior to use. Zinc chloride (99.999% trace metals basis), selenium (99.99% trace metals basis), decyl magnesium bromide in diethyl ether, and iodine monochloride (ICl) in dichloromethane were purchased from Sigma–Aldrich Inc. 1-Methyl-2-pyrrolidone (NMP) and sulfuryl chloride (SO₂Cl₂) were purchased from Wako chemicals. Lithium chloride, *n*-BuLi in hexane, *t*-BuLi in pentane, and iodine, and all anhydrous solvents were purchased from KANTO chemicals.

General for Synthesis and Characterization

All reactions were carried out under an atmosphere of either nitrogen or argon. Air- and moisture-sensitive liquids and solutions were transferred via a syringe or a Teflon cannula. Analytical thin-layer chromatography (TLC) was performed on glass plates with 0.25 mm 230–400 mesh silica gel containing a fluorescent indicator (Merck Silica gel 60 F254). TLC plates were visualized by either exposure to ultraviolet lamp (254 nm and 365 nm) or by dipping with 10% phosphomolybdic acid in ethanol and then heating on a hot plate. Flash column chromatography was performed on Kanto silica gel 60. Open column chromatography was performed on Wakogel C-200 (75–150 μ m). All NMR spectra were recorded on a JEOL ECA600 and JEOL ECS400 spectrometers. Chemical shifts are reported in parts per million (ppm, δ scale) from residual protons in the deuterated solvent for ¹H NMR (δ 7.26 ppm for chloroform, δ 5.93 ppm for 1,1,2,2-tetrachloroethane) and from the solvent carbon for ¹³C NMR (δ 77.16 ppm for chloroform and δ 73.78 ppm for 1,1,2,2-tetrachloroethane). The data were presented in the following format: chemical shift, multiplicity (s = singlet, d = doublet, t = triplet, m = multiplet), coupling constant in Hertz (Hz), signal area integration in natural numbers, assignment (*italic*). Mass spectra were measured on a JEOL JMS-T100LC APCI/ESI mass spectrometer. Melting points and elemental analyses were collected on a Mettler Toledo MP70 Melting Point System and J-Science Lab JM10 MICRO CORDER, respectively.

Zinc chloride solution

An oven-dried Schlenk tube was charged with zinc chloride (52.3 g, 384 mmol), and the tube was heated under evacuation until zinc chloride completely melted. After cooling to room temperature, dry THF (384 mL) was added to give ca. 1.0 M zinc chloride solution.

LiTMP

To a solution of TMP (65.3 mL, 384 mmol) in THF (384 mL) was added *n*-BuLi (1.60 M hexane solution, 240 mL, 384 mmol) at $-78\text{ }^{\circ}\text{C}$. After stirred at $0\text{ }^{\circ}\text{C}$ for 30 min, LiTMP solution was generated.

t-Bu₂Zn(TMP)Li¹⁻³

To a solution of ZnCl₂ (1.0 M in THF, 274 mL, 274 mmol) was added *t*-BuLi (1.71 M pentane solution, 434 mL, 768 mmol) at $0\text{ }^{\circ}\text{C}$, and the mixture was stirred at $0\text{ }^{\circ}\text{C}$ for 30 min. The prepared *t*-Bu₂Zn was transferred via a Teflon cannula to a solution of LiTMP at $-78\text{ }^{\circ}\text{C}$. After stirred at $0\text{ }^{\circ}\text{C}$ for 30 min, *t*-Bu₂Zn(TMP)Li solution was prepared.

SeCl₂⁴

To selenium powder (474 mg, 6.0 mmol, 1.20 mol amt.) was added SO₂Cl₂ (810 mg, 6.0 mmol, 1.20 mol amt.) at ambient temperature. The mixture was stirred for 10 min, and 12 mL of THF was added. The solution was stirred for 1 h to give a clear brownish red solution of SeCl₂.

7-Bromo-2-trimethylsilylnaphthalene

To a suspension of 2,7-dibromonaphthalene (50.0 g, 175 mmol) and *N,N,N,N*-tetramethylethylenediamine (28.7 mL, 193 mmol, 1.10 mol amt.) in Et₂O (350 mL) was added *n*-BuLi (1.60 M in hexane, 113 mL, 180 mmol, 1.03 mol amt.) dropwise over 20 min at $-78\text{ }^{\circ}\text{C}$. After the mixture was stirred at that temperature for 1.5 h, a solution of trimethylsilyl chloride (26.7 mL, 210 mmol, 1.20 mol amt.) in Et₂O (210 mL) was added at $-78\text{ }^{\circ}\text{C}$. After stirring at that temperature for 3 h, the reaction was quenched by H₂O. The organic layer was separated with hexane, washed with brine, dried over MgSO₄. After removing the solvent was removed *in vacuo*, the crude material was purified by distillation ($151\text{ }^{\circ}\text{C}$, 2.9 Torr) to afford the titled compound (39.6 g, 142 mmol, 81%) as white solid. m.p.: $41.7\text{--}42.2\text{ }^{\circ}\text{C}$. ¹H NMR (400 MHz, CDCl₃): δ 0.34 (s, 9H, Si(CH₃)₃), 7.54 (dd, $J = 8.0\text{ Hz}$ and 1.6 Hz , 1H, ArH), 7.60 (d, $J = 8.0\text{ Hz}$, 1H, ArH), 7.68 (d, $J = 8.0\text{ Hz}$, 1H, ArH), 7.78 (d, $J = 8.0\text{ Hz}$, 1H, ArH), 7.90 (s, 1H, ArH), 8.01 (d, $J = 1.6\text{ Hz}$, 1H, ArH). ¹³C NMR (100 MHz, CDCl₃): δ -1.05 , 119.77 , 126.90 , 129.47 , 129.62 , 130.16 , 130.35 , 132.05 , 132.84 , 134.03 , 139.54 . TOF HRMS (APCI+): Calcd for C₁₃H₁₆⁷⁹BrSi [M+H] 278.0121, found, 278.0117. Anal. Calcd for C₁₃H₁₅BrSi: C, 55.91; H, 5.41. Found C, 56.19; H, 5.68.

2-Bromo-3-iodo-7-trimethylsilylnaphthalene (2)

To a suspension of *t*-Bu₂Zn(TMP)Li (384 mmol, 2.4 mol amt.) was added a solution of compound **1** (44.7 g, 160 mmol) in THF (240 mL) dropwise at $-78\text{ }^{\circ}\text{C}$. After stirring at $-20\text{ }^{\circ}\text{C}$ for 12 h, a solution of iodine (284 g, 1.12 mol, 7.0 mol amt.) in THF (373 mL) was added at $-78\text{ }^{\circ}\text{C}$. After

stirring at this temperature for 2 h, the reaction was quenched by Na₂S₂O₃ aqueous solution. The organic phase was separated with ethyl acetate, washed with brine, and dried over MgSO₄. After removing the solvent in vacuo, the crude material was passed through a short pad of silica gel column employing hexane as an eluent. After removing the solvent *in vacuo*, the crude materials were purified by recrystallization from hexane/chloroform to afford the titled compound **2** (40.2 g, 99.2 mmol, 62%) as white solid. m.p.: 79.2–80.0 °C. ¹H NMR (400 MHz, CDCl₃): δ 0.33(s, 9H, Si(CH₃)₃), 7.61 (d, *J* = 8.0 Hz, 1H, Ar*H*), 7.67 (d, *J* = 8.0 Hz, 1H, Ar*H*), 7.86 (s, 1H, Ar*H*), 8.15 (s, 1H, Ar*H*), 8.39 (s, 1H, Ar*H*). ¹³C NMR (100 MHz, CDCl₃): δ –1.12, 98.58, 125.62, 126.01, 131.04, 131.17, 132.65, 133.26, 133.46, 139.47, 140.32. TOF HRMS (APCI+): Calcd for C₁₃H₁₅⁷⁹BrSi [M+H] 403.9087, found, 403.9070. Anal. Calcd for C₁₃H₁₄BrSi: C, 38.54; H, 3.48. Found C, 38.40; H, 3.73.

3,3'-Dibromo-6,6'-bis(trimethylsilyl)-2,2'-binaphthalene (**3**)

To a suspension of compound **2** (6.89 g, 17.0 mmol) in THF (68 mL, 0.25 M) was added *i*-PrMgBr (1.0 M in THF, 17.9 mL, 17.9 mmol, 1.03 mol amt.) at –78 °C. After stirring at that temperature for 30 min, a solution of ZnCl₂ (1.0 M in THF, 17.9 mL, 17.9 mmol, 1.03 mol amt.) was added at that temperature. After warming to ambient temperature and stirring for 30 min, LiCl (0.5 M in THF, 35.8 mL, 35.8 mmol, 1.03 mol amt.) was added and stirred for 30 min at ambient temperature. To the resulting colorless solution, *N*-methyl-2-pyrrolidone (17 mL), 2-bromo-3-iodo-7-trimethylsilylnaphthalene (6.54 g, 16.2 mmol, 0.95 mol amt.) and tetrakis(triphenylphosphine)palladium(0) (374 mg, 0.320 mmol, 2 mol%) was added. After the mixture was stirred at ambient temperature for 16 h, the reaction was quenched by MeOH. The resulting white precipitate was collected by filtration. After dissolving the collected white solid in chloroform, the organic materials were passed through a short pad of silica gel column. After reducing the solvent to c.a. 10 mL in vacuo, addition of MeOH afforded the titled compound **3** (7.21 g, 13.0 mmol, 80% yield) as white solid, which was collected by filtration. After removing the solvent of the combined filtrate *in vacuo*, the crude material was purified by silica gel column chromatography (hexane: chloroform = 98:2 to 95:5) to afford the additional titled compound **3** (1.35 g, 2.4 mmol, 15% yield). Total yield: 95%. m.p.: 256.2–256.9 °C. ¹H NMR (400 MHz, CDCl₃): δ 0.37 (s, 18H, Si(CH₃)₃), 7.66 (d, *J* = 8.0 Hz, 2H, Ar*H*), 7.77 (s, 2H, Ar*H*), 7.81 (d, *J* = 8.0 Hz, 2H, Ar*H*), 7.99 (s, 2H, Ar*H*), 8.21 (s, 2H, Ar*H*). ¹³C NMR (100 MHz, CDCl₃): δ –1.00, 121.87, 127.05, 129.98, 130.81, 131.24, 132.22, 132.70, 133.52, 139.96, 140.01. TOF HRMS (APCI+): Calcd for C₂₆H₂₉⁷⁹Br₂Si₂ [M+H] 554.0091, found, 554.0076. Anal. Calcd for C₂₆H₂₈Br₂Si₂: C, 56.12; H, 5.07. Found C, 56.12; H, 5.18.

3,9-Bis(trimethylsilyl)dinaphtho[2,3-*b*:2',3'-*d*]selenophene (**4**)

To a white suspension of compound **3** (2.78 g, 5.00 mmol) in Et₂O (25 mL) was added *n*-BuLi in hexane (1.60 M, 6.44 mL, 10.3 mmol, 2.05 mol amt.) at –78 °C. After warming to 0 °C and stirring for 1 h, the prepared SeCl₂ was transferred by Teflon cannula to the resulting brown solution at –78 °C. After stirring at –78 °C for 2 h, the reaction was quenched with H₂O. The organic layer was extracted with CH₂Cl₂, washed with brine, dried over MgSO₄. After removing the solvent *in vacuo*, the crude material was purified by silica gel column chromatography (hexane: dichloromethane = 100:0 to 95:5) to afford the title compound **4** (1.52 g, 3.20 mmol, 64% yield). m.p.: 271.0–271.9 °C. ¹H NMR (400 MHz, CDCl₃): δ 0.38 (s, 18H, Si(CH₃)₃), 7.64 (d, *J* = 8.0 Hz, 2H, ArH), 8.01 (d, *J* = 8.0 Hz, 2H, ArH), 8.02 (s, 2H, ArH), 8.27 (s, 2H, ArH), 8.68 (s, 2H, ArH). ¹³C NMR (100 MHz, CDCl₂CDCl₂): δ –0.84, 121.66, 124.61, 127.62, 129.81, 131.42, 132.72, 132.87, 136.46, 137.52, 139.31. HRMS (APCI+): Calcd for C₂₆H₂₉SeSi₂ [M+H] 477.0973, found, 477.0974. Anal. Calcd for C₂₆H₂₈SeSi₂: C, 65.66; H, 5.93. Found C, 65.35; H, 5.85.

3,9-Diiododinaphtho[2,3-*b*:2',3'-*d*]selenophene (**I-DNS-VW**)

To a pale yellow suspension of **4** (686 mg, 1.60 mmol) in dichloromethane (16 mL) was added ICl in dichloromethane (1.0 M, 3.68 mL, 3.68 mmol, 2.3 mol amt.) was at –78 °C. After stirring at 0 °C for 2 h, the reaction was quenched by Na₂S₂O₃ aqueous solution and warmed to room temperature. The yellow precipitate was collected by filtration. After dissolving the organic material in 1,2-dichlorobenzene at 120 °C, the solution was passed through a short pad of Celite to remove the insoluble materials. After removing the solvent *in vacuo*, the title compound **I-DNS-VW** (783 mg, 1.46 mmol, 91% yield) was obtained as yellow solid. m.p.: 343.7–344.5 °C. ¹H NMR (400 MHz, CDCl₂CDCl₂): δ 7.72 (s, 4H, ArH), 8.10 (s, 2H, ArH), 8.21 (s, 2H, ArH), 8.60 (s, 2H, ArH). ¹³C NMR (100 MHz, CDCl₂CDCl₂, 125 °C): δ 92.46, 121.75, 123.16, 129.93, 130.04, 134.33, 134.79, 135.57, 137.51, 137.62. TOF HRMS (APCI+): Calcd for C₂₀H₁₁SeI₂ [M+H] 584.8115, found, 584.8114. Anal. Calcd for C₂₀H₁₀SeI₂: C, 41.20; H, 1.73. Found C, 41.11; H, 1.86.

3,9-Didecyldinaphtho[2,3-*b*:2',3'-*d*]selenophene (**C₁₀-DNS-VW**)

To a colorless solution of decylmagnesium bromide in diethylether (1.0 M, 720 μL, 0.720 mmol, 2.4 mol amt.) in toluene (3.0 mL) was added ZnCl₂ in THF (1.0 M, 750 μL, 0.750 mmol, 2.5 mol amt.) at 0 °C to prepare organozinc reagent. After stirring at room temperature for 10 min, **I-DNS-VW** (175 mg, 0.300 mmol, 1.00 mol amt.) and PdCl₂(dppf)•CH₂Cl₂ (9.8 mg, 0.012 mmol, 4 mol%) were successively added at room temperature. The resulting brown suspension was warmed to 70 °C and stirred for 12 h. After cooling to room temperature, the reaction was quenched with H₂O. The organic layer was separated by dichloromethane and washed with brine, and dried over MgSO₄. After removing the solvent *in vacuo*, the crude material was purified by silica gel column

chromatography (hexane: CH₂Cl₂ = 100:0 to 95:5) to afford the titled compound **C₁₀-DNS-VW** as a white solid (172 mg, 0.281 mmol, 93% yield). m.p.: 163.9–164.8 °C. ¹H NMR (400 MHz, CDCl₂CDCl₂): δ 0.82 (t, *J* = 6.4 Hz, 6H, CH₃), 1.18–1.36 (m, 28H, (CH₂)₇), 1.67 (q, *J* = 7.2 Hz, 4H, ArCH₂CH₂), 2.75 (t, *J* = 7.2 Hz, 4H, ArCH₂), 7.35 (d, *J* = 8.4 Hz, 2H, ArH), 7.57 (s, 2H, ArH), 7.90 (d, *J* = 8.4 Hz, 2H, ArH), 8.14 (s, 2H, ArH), 8.57 (s, 2H, ArH). ¹³C NMR (100 MHz, CDCl₂CDCl₂): δ 14.37, 22.85, 29.46, 29.51, 29.68, 29.74, 29.77, 31.39, 32.02, 36.32, 121.19, 123.73, 125.10, 127.52, 128.37, 129.77, 133.52, 136.31, 136.57, 141.50. HRMS (APCI+): Calcd for C₄₀H₅₃Se [M+H] 613.3312, found, 613.3293. Anal. Calcd for C₄₀H₅₂Se: C, 78.53; H, 8.57. Found C, 78.56; H, 8.76.

Dinaphtho[2,3-*b*:2',3'-*d*]selenophene (DNS-V)

The target compound was prepared according to a modified reported procedure.¹ To a flame-dried Schlenk tube was added **I-DNS-VW** (30.0 mg, 0.0514 mmol, 1.0 equiv.) and anhydrous THF (1 mL, 0.05 M), and the light-yellow mixture was purged by argon for 5 min. Subsequently, PdCl₂(dppf) (1.88 mg, 0.00257 mmol, 5 mol%), TMEDA (13.1 mg, 0.113 mmol, 2.2 equiv.), and NaBH₄ (4.86 mg, 0.129 mmol, 2.5 equiv.) were sequentially added to the system. The reaction mixture was stirred at room temperature under argon for 5 h before it was quenched by water. The compound was extracted by EtOAc and dried over Na₂SO₄. The crude was purified by column chromatography using hexanes/CHCl₃ as eluents (3:1 v/v) to afford the target compound as a light-yellow solid (15.0 mg, 0.01452 mmol, 88% yield). ¹H NMR (400 MHz, CDCl₂CDCl₂): δ 8.66 (s, 2H, ArH), 8.24 (s, 2H, ArH), 8.03–8.01 (t, *J* = 5.6 Hz, 3.2 Hz, 2H, ArH), 7.86–7.83 (s, *J* = 3.6 Hz, 5.6 Hz, 2H, ArH), 7.53–7.50 (t, *J* = 4.0 Hz, 4.4 Hz, 4H, ArH). ¹³C NMR (100 MHz, CDCl₂CDCl₂, 100 °C): δ 137.13, 136.28, 133.37, 131.26, 128.31, 126.54, 126.31, 125.39, 124.05, 121.35. TOF HRMS (APCI+): Calcd for C₂₀H₁₂Se [M+H] 333.0182, found, 333.0177.

2. Thermal Analyses: Thermogravimetric Analyses (TGA)

TGA measurements were carried out with a Rigaku Thermo Plus EVO II TG 8120. Sample was placed in an aluminum pan and heated at the rate of 5 K min^{-1} under N_2 purge at a flow rate of 100 mL min^{-1} . Al_2O_3 was used as the reference material. The TG data of **DNS-V** and **C₁₀-DNS-VW** along with **DNF-V**, **DNT-V**, **C₁₀-DNF-VW**, and **C₁₀-DNT-VW** are depicted in Figure S1 and S2, respectively.

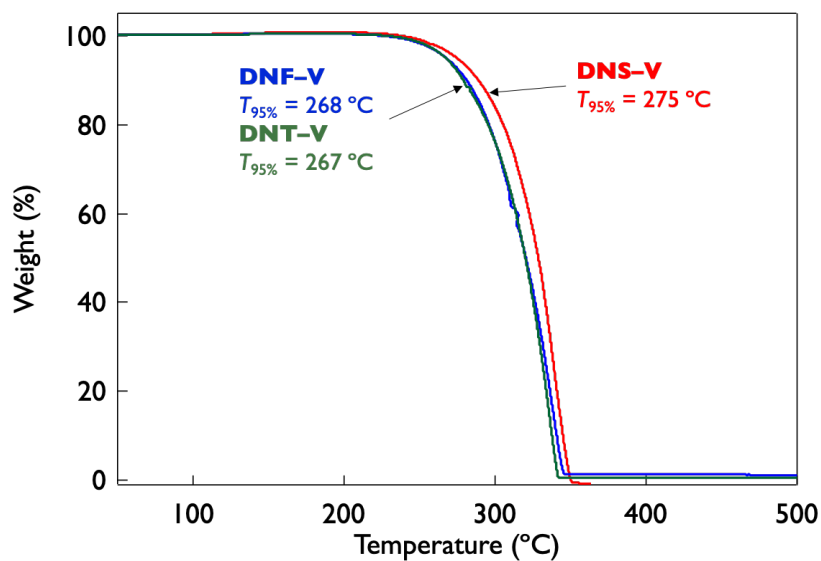


Figure S1. TGA charts of **DNF-V**, **DNT-V** and **DNS-V**.

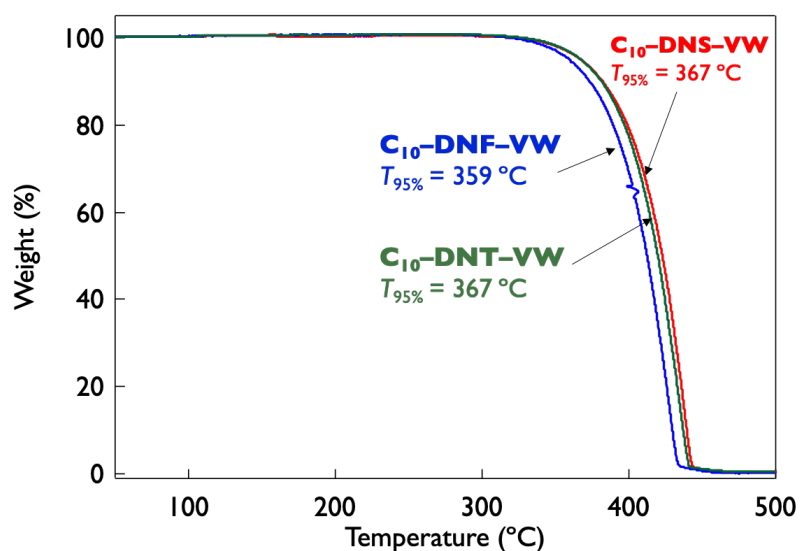


Figure S2. TGA charts of **C₁₀-DNF-VW**, **C₁₀-DNT-VW** and **C₁₀-DNS-VW**.

3. Ionization Potentials

Photoelectron yield spectroscopy (PYS) was performed on a Sumitomo Heavy Industries Advanced Machinery PYS-202. For PYS measurements, thin films (*ca.* 100 nm) of unsubstituted and decyl-substituted V-shaped derivatives were thermally evaporated on ITO coated quartz substrates and measurements were performed in vacuum (Figure S3-4). Table 1 summarized their ionization potentials and calculated HOMO level of **DNS-V** and **C₁₀-DNS-VW** along with **DNF-V**, **DNT-V**, **C₁₀-DNF-VW**, and **C₁₀-DNT-VW**.

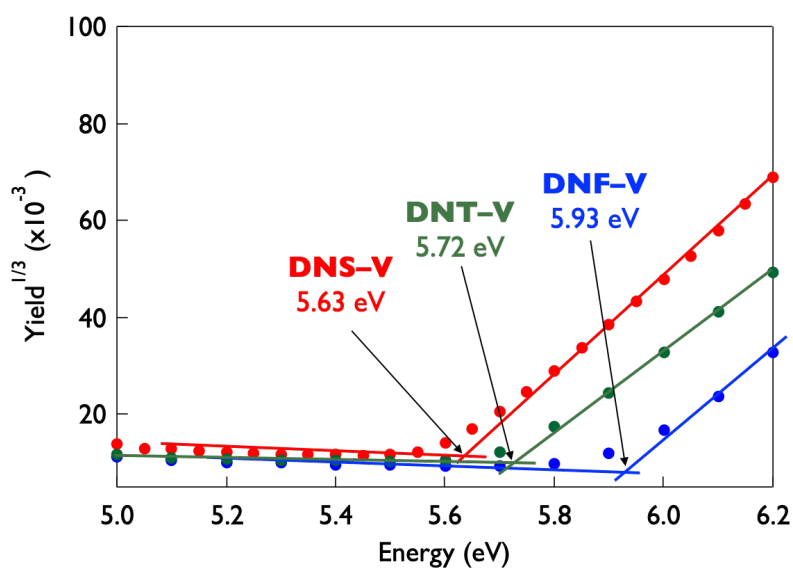


Figure S3. Photoelectron yield spectra of **DNF-V**, **DNT-V** and **DNS-V** in thin films after light illumination from a D₂ lamp in vacuo.

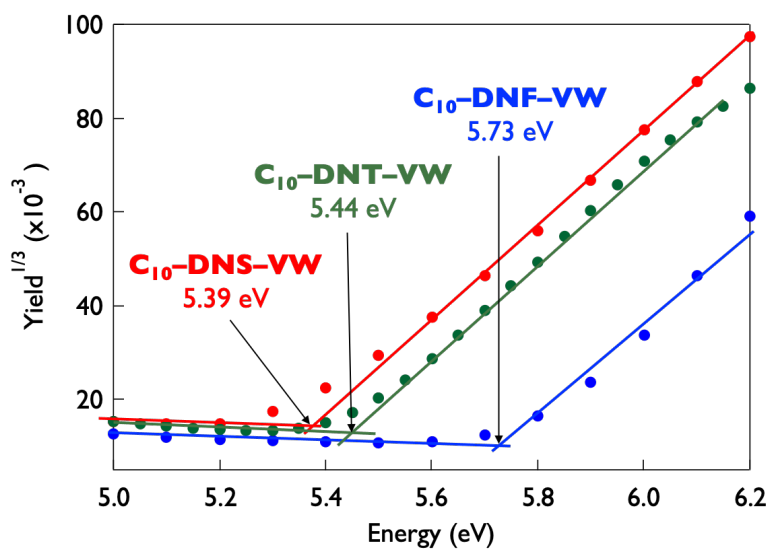


Figure S4. Photoelectron yield spectra of **C₁₀-DNF-VW**, **C₁₀-DNT-VW** and **C₁₀-DNS-VW** in thin films after light illumination from a D₂ lamp in vacuo.

Table S1. Ionization potentials of unsubstituted and decyl-substituted V-shaped derivatives.

Compounds	Ionization potentials (eV)	Calculated HOMO (eV) ^a
DNF-V	5.93	−5.80
DNT-V	5.72	−5.62
DNS-V	5.63	−5.55
C₁₀-DNF-VW	5.73	−5.72 ^b
C₁₀-DNT-VW	5.44	−5.54 ^b
C₁₀-DNS-VW	5.39	−5.48 ^b

^a HOMO levels were calculated at the B3LYP/6-311G(d)//B3LYP/6-31G(d) level of theory.

^b Me-substituted derivatives were applied to use for calculation.

4. Single-Crystal Analyses

Single crystals of **DNS-V** were obtained by horizontal physical vapor transport (PVT) technique. The structural data were successfully collected by single crystal X-ray diffraction (SC-XRD) analysis (Figure S5). The length and diameter of Pyrex tube used are 120 cm and 2 cm, respectively. Under an Ar carrier gas flow, source and crystallization-zone were heated at a certain temperature to produce their single crystals. Flow rate of Ar carrier gas and source and crystallization-zone temperature were summarized in Table S2.

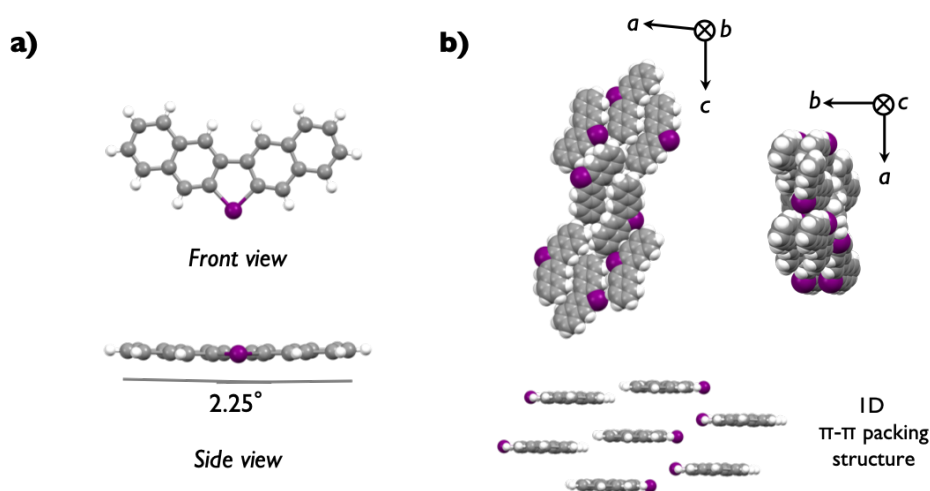


Figure S5. a) Molecular structure and b) aggregated structure of **DNS-V** in single-crystal structure.

Table S2. PVT conditions for crystallization of **DNS-V**.

Source temp. (°C)	Crystallization-zone temp. (°C)	Ar flow rate (ccm)
230	170	50

5. Differential Scanning Calorimetric (DSC) Analyses

DSC measurements were carried out with a Rigaku Thermo Plus EVO II DSC8270. Sample was placed in an aluminum pan and heated at the rate of 5 K min^{-1} , under N_2 purge at a flow rate of 100 mL min^{-1} . Al_2O_3 was used as the reference material. The DSC data are depicted in Figure S6–7.

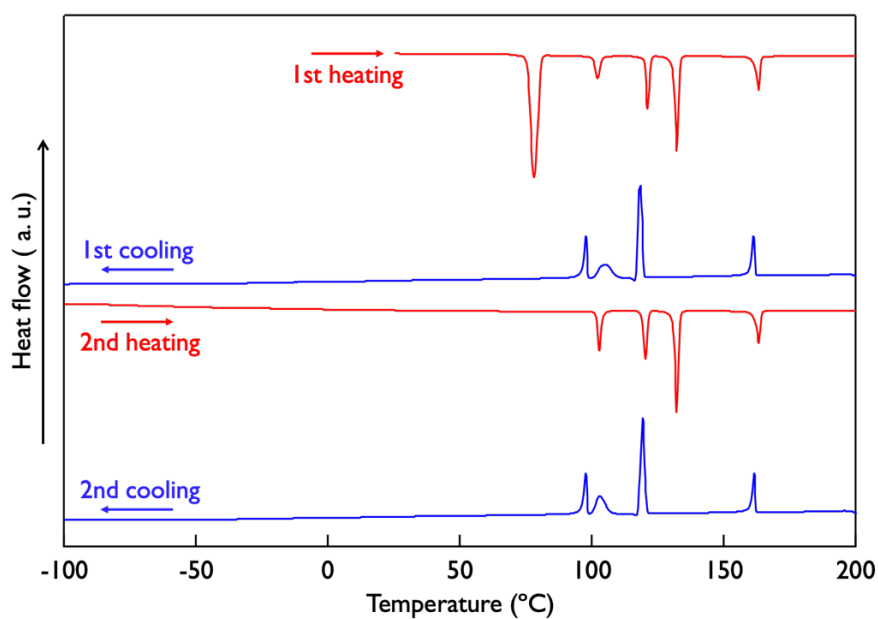


Figure S6. DSC charts of C₁₀-DNS-VW at a scanning rate of 5 K min^{-1} .

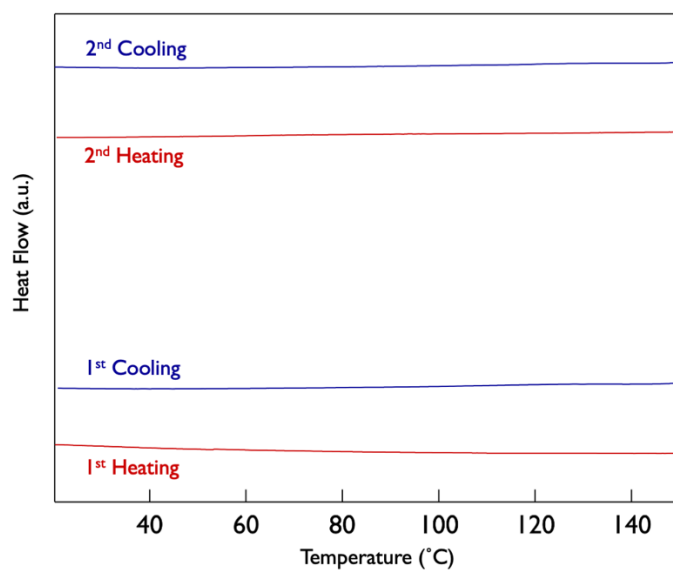


Figure S7. DSC charts of DNS-V at a scanning rate of 5 K min^{-1} .

6. Powder X-ray Analyses

A powder X-ray diffraction (PXRD) pattern of **C₁₀–DNS–VW** was recorded at 303 K in transmission mode on a diffractometer equipped with an imaging plate detector at the RIKEN Materials Science Beamline (BL44B2) at SPring-8. Measurement conditions were as followed: capillary diameter: 0.3 mm; synchrotron radiation $\lambda = 1.08 \text{ \AA}$; 2θ range: $1.0\text{--}77.58^\circ$; step width: 0.01° .⁵

Phase transition from **C₁₀–DNS–VW-colorless** phase to **C₁₀–DNS–VW-yellow** phase.

The powder sample was prepared as follow. **C₁₀–DNS–VW** was recrystallized by isopropanol vapor diffusion to the toluene solution to form the colorless crystals. Then, the colorless crystals were carefully crashed and encapsulated in the glass capillary under vacuum. A PXRD pattern of the obtained sample at 30 °C was confirmed to be in good agreement with the simulated powder pattern of **C₁₀–DNS–VW-colorless** phase. A completely different diffraction pattern was observed in the heating process at 98 °C (at a rate of 10 K min^{-1}), indicating the phase transition from **C₁₀–DNS–VW-colorless** phase to **C₁₀–DNS–VW-yellow** phase (Figure S8). During the subsequent cooling process to 30 °C, no drastic change was observed. Note that a weak diffraction peak was detected at 2.64° showing the existence of small amount of **C₁₀–DNS–VW-colorless**, whereas most of the sample remained in the yellow crystal phase.

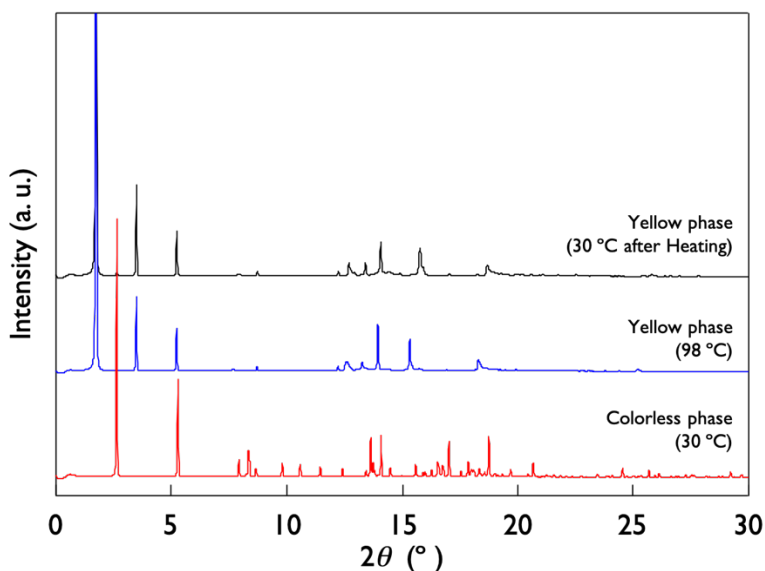


Figure S8. PXRD patterns of **C₁₀–DNS–VW**: (Bottom) The initial colorless phase at 30 °C; (middle) yellow phase at 98 °C in the heating process; and (top) the yellow phase at 30 °C in the subsequent cooling process.

Variant temperature PXRD measurement and the liquid crystallinity of C₁₀-DNS-VW.

The colorless crystals were carefully crashed and encapsulated in the glass capillary under vacuum. The capillary was heated to 98 °C at a rate of 10 K min⁻¹ to transform the colorless crystals to the yellow crystals. The PXRD measurements were performed in the range of 30 °C to 180 °C in the heating process (Figure S9) and in the subsequent cooling process (Figure S10) at a rate of 10 K min⁻¹. In Figure S9 and S10, many diffraction peaks were observed below 125 °C, indicating the formation of crystalline phases in the temperature range. However, only one diffraction peak at 1.78° and broad peak around 13.7° were obtained at 145 °C, showing that C₁₀-DNS-VW exhibits a liquid crystalline phase in the high temperature region. Polarizing optical microscopic observation supports the formation of smectic A phase in the temperature region (Figure S11). On further heating, a phase transition to the isotropic liquid phase occurs because no obvious peaks were detected at 180 °C.

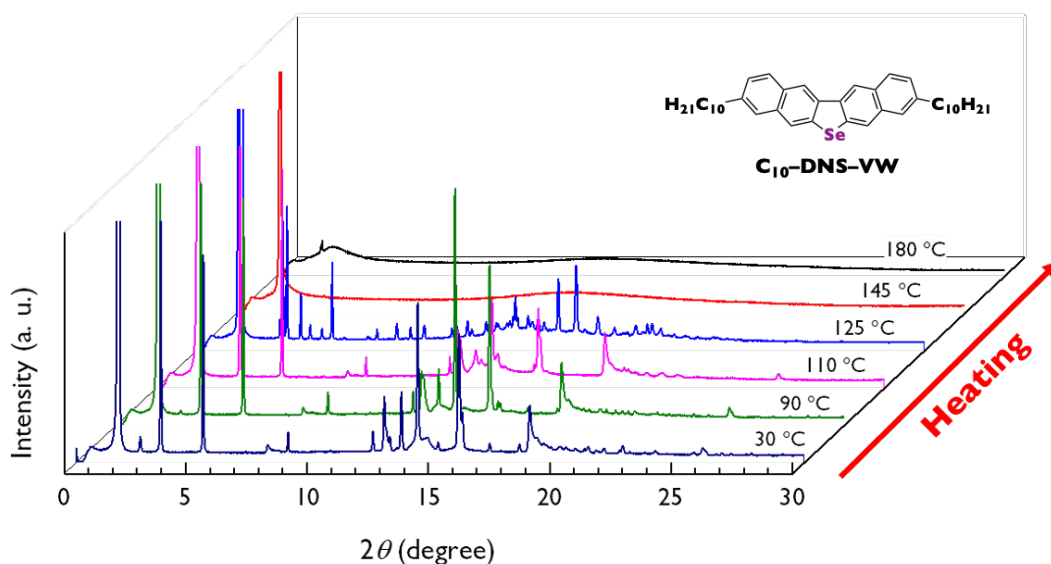


Figure S9. PXRD patterns of C₁₀-DNS-VW in the heating process at a rate of 10 K min⁻¹.

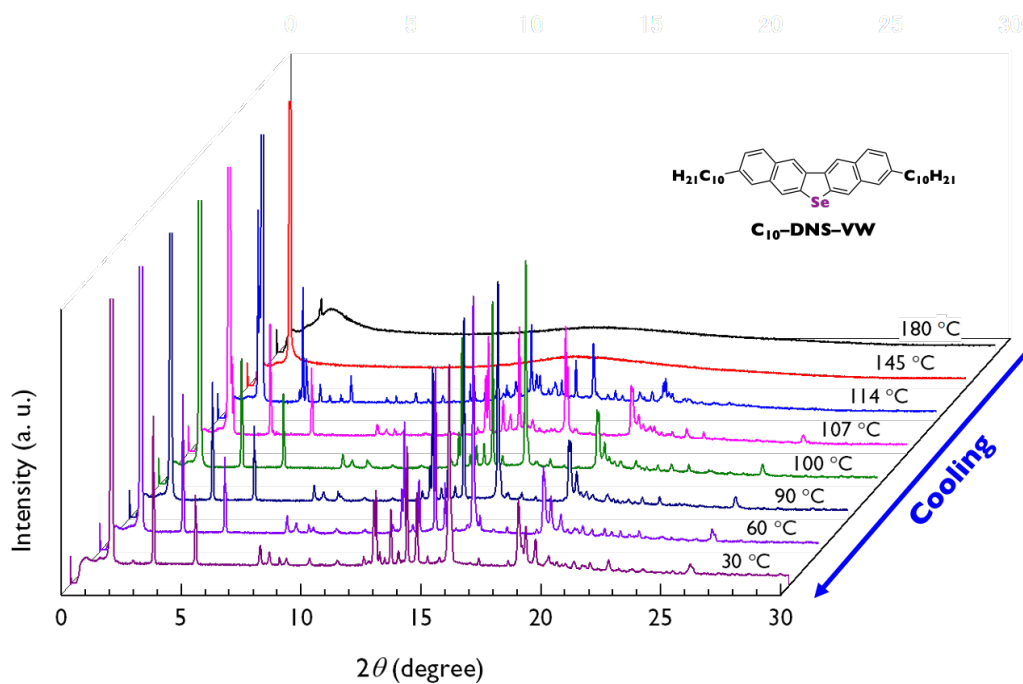


Figure S10. PXRD patterns of **C₁₀-DNS-VW** in the cooling process at a rate of 10 K min⁻¹.

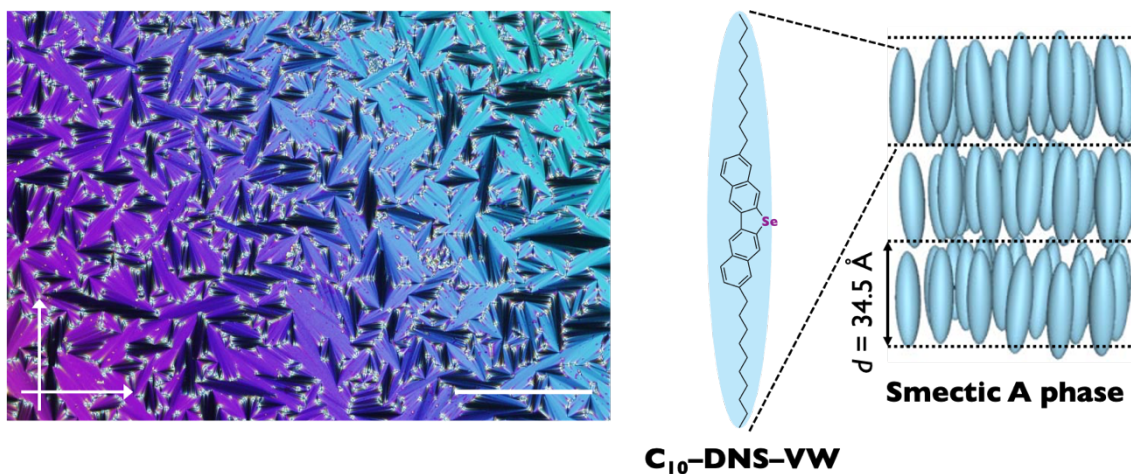


Figure S11. (Left) A polarizing optical microscopic image of **C₁₀-DNS-VW** at 140 °C in the smectic A phase. Arrows indicate the directions of polarizer and analyzer axes. Scale bar: 200 μm. (right) A molecular structure of **C₁₀-DNS-VW** and schematic illustration of the smectic A phase.

Vapor-induced phase transition from C_{10} -DNS-VW-yellow phase to C_{10} -DNS-VW-colorless phase.

As an initial sample, C_{10} -DNS-VW was recrystallized by IPA vapor diffusion to the toluene solution to form the colorless crystals, which were subsequently carefully crashed. Next, to obtain the sample in the yellow phase, the colorless crystals were heated to 98 °C at a rate of 10 K min⁻¹. Finally, to recover the colorless phase, the yellow sample was exposed to the saturated CHCl₃ vapor at room temperature for overnight. The three samples obtained in each crystalline phase were encapsulated in the glass capillary under vacuum and PXRD measurements were performed for the three samples (Figure S12).

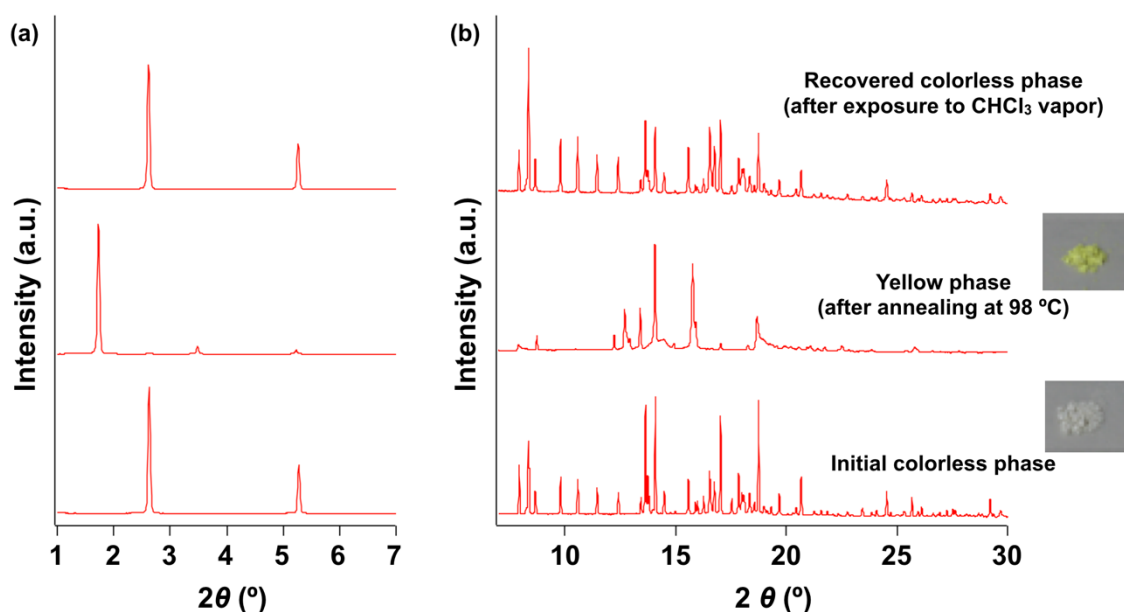


Figure S12. PXRD patterns of C_{10} -DNS-VW: (a) in the small angle region; (b) wide angle region obtained at 30 °C using synchrotron radiation. (Bottom) the initial colorless phase, (middle) the yellow phase after heating, and (top) the recovered colorless phase after exposure to the CHCl₃ vapor.

7. Powder UV-vis Absorption Spectra.

Powder UV-vis absorption spectra of **C₁₀–DNS–VW**-*colorless* and -*yellow* were measured in KBr matrix, along with **C₁₀–DNS–VW** in 1,2-dichloroethane in comparison (Figure S13).

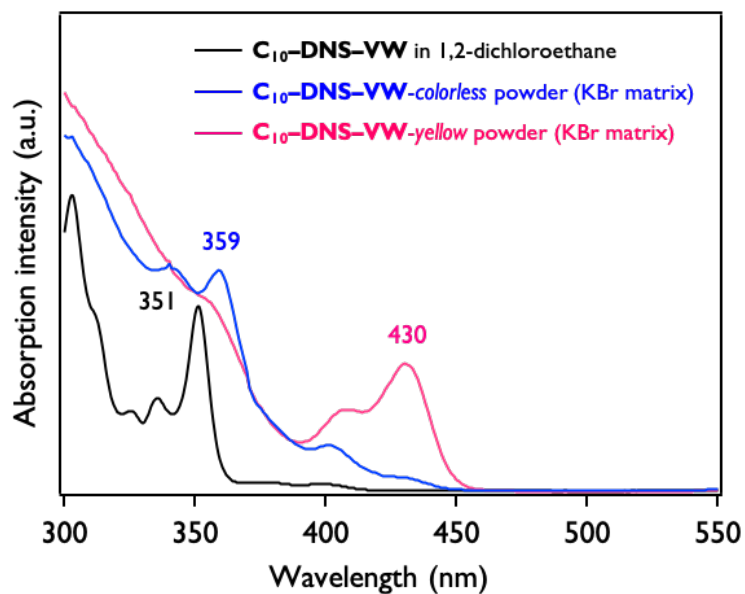


Figure S13. Powder UV-vis absorption spectra of **C₁₀–DNS–VW** in KBr matrix.

8. UV-vis and Time-Dependent UV-vis Absorption Spectra in Solution and Deposited Thin Film

UV-vis absorption spectra were measured with a JASCO V-570 spectrometer. Samples in solution were prepared in degassed 1,2-dichloroethane. Thin films were prepared by vacuum deposition with the thickness of *ca.* 100 nm on quartz substrates. The prepared samples in solution and thin films were stored under ambient atmosphere (room temperature and room light) between measurements. Spectra had not change over at least 2 weeks for solution (Figure S14) and 4 weeks for deposited film (Figure S15), which indicates **C₁₀–DNS–VW** is chemically stable in both solution and solid state.

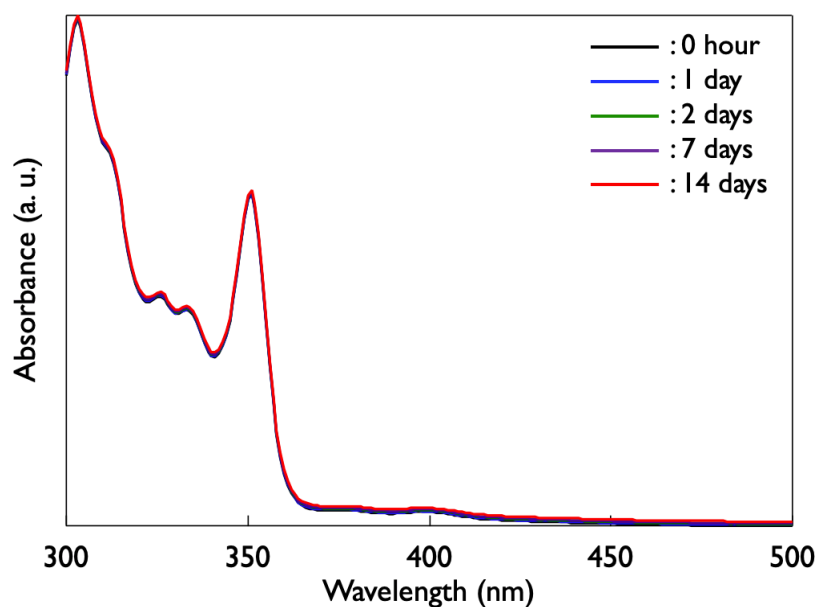


Figure S14. Time-dependent absorption spectra of **C₁₀–DNS–VW** in 1,2-dichloroethane.

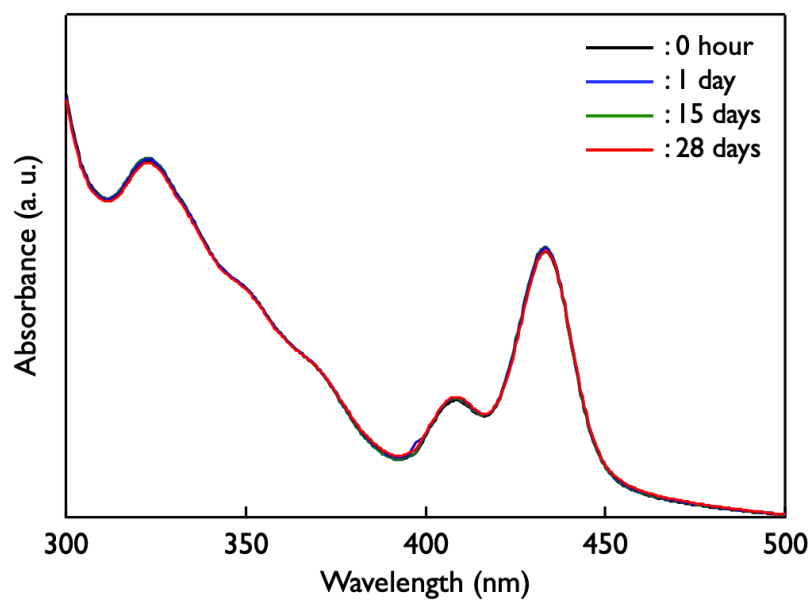


Figure S15. Time-dependent absorption spectra of a *ca.*100-nm-thick deposited film of C₁₀-DNS-VW.

9. Theoretical Calculations

9.1 LUMO, HOMO, and NHOMO Energy Levels

Theoretical calculations of lowest unoccupied molecular orbital (LUMO), highest occupied molecular orbital (HOMO), next highest occupied molecular orbitals (NHOMO) for unsubstituted V-shaped derivatives (**DNF-V**, **DNT-V** and **DNS-V**) were conducted for a single molecule at the B3LYP/6-31G(d), 6-311G(d), cc-pVDZ, and cc-pVTZ levels of theory using the SPARTAN 16 package, Wavefunction Inc (Table S3).

Table S3. LUMO, HOMO and NHOMO energy levels of **DNF-V**, **DNT-V** and **DNS-V**, calculated at the B3LYP-functional 6-31G(d), 6-311G(d), cc-pVDZ and cc-pVTZ levels of theory.

Compounds	LUMO, HOMO and HOMO-LUMO gap	Energy levels and gaps			
		B3LYP/ 6-31G(d)	B3LYP/ 6-311G(d)	B3LYP/ cc-pVDZ	B3LYP/ cc-pVTZ
DNS-V	LUMO	-1.63	-1.90	-1.85	-1.95
	HOMO	-5.33	-5.55	-5.48	-5.58
	NHOMO	-5.62	-5.85	-5.78	-5.89
	HOMO-LUMO gap	3.70	3.65	3.63	3.63
	HOMO-NHOMO gap	0.29	0.30	0.30	0.30
DNF-V	LUMO	-1.65	-1.92	-1.87	-1.97
	HOMO	-5.55	-5.80	-5.72	-5.83
	NHOMO	-5.66	-5.89	-5.83	-5.93
	HOMO-LUMO gap	3.90	3.88	3.85	3.86
	HOMO-NHOMO gap	0.11	0.09	0.11	0.10
DNT-V	LUMO	-1.64	-1.91	-1.86	-1.96
	HOMO	-5.41	-5.62	-5.56	-5.64
	NHOMO	-5.63	-5.87	-5.80	-5.90
	HOMO-LUMO gap	3.77	3.71	3.70	3.68
	HOMO-NHOMO gap	0.22	0.25	0.24	0.26

9.2 LUMO and HOMO Energy Levels, HOMO-LUMO Gaps and Total Energies of C₁₀-DNS-VW-*yellow* and C₁₀-DNS-VW-*colorless*.

Theoretical calculations of LUMO and HOMO energy levels, HOMO-LUMO gaps for C₁₀-DNS-VW-*yellow*- and C₁₀-DNS-VW-*colorless*-based molecular structures were conducted at the B3LYP/6-311G(d) levels using the SPARTAN 16 package, Wavefunction Inc (Figure S16).

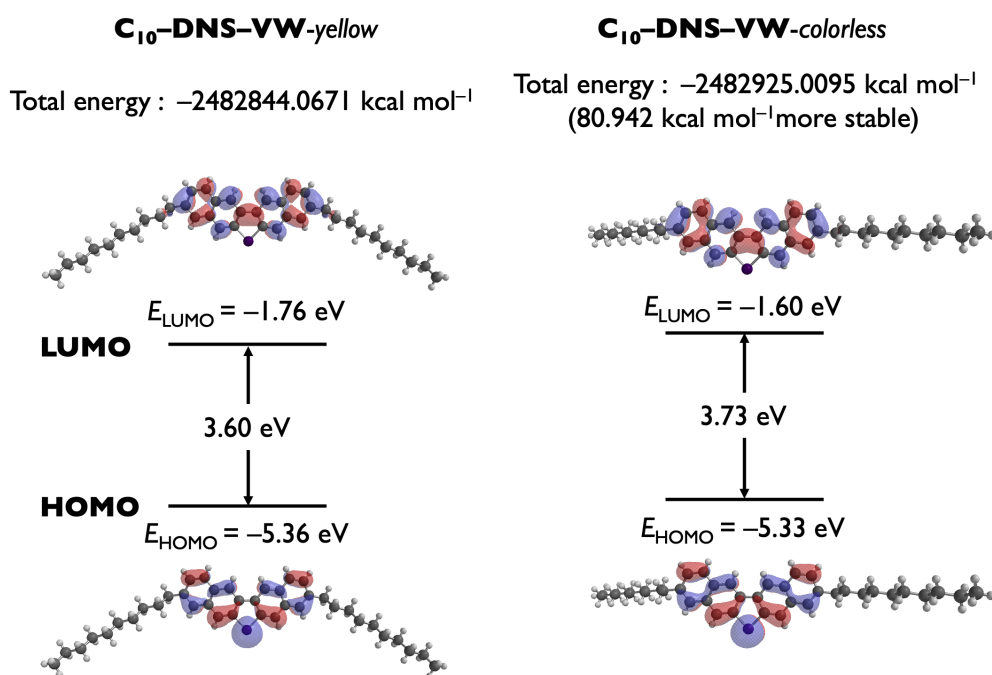


Figure S16. Total energies, LUMO, HOMO and their energy levels, HOMO-LUMO gaps of C₁₀-DNS-VW-*yellow* and C₁₀-DNS-VW-*colorless* at the B3LYP/6-311G(d) level of theory.

9.3 Intermolecular interaction energy of C₁₀-DNS-VW-*yellow* and C₁₀-DNS-VW-*colorless*.

Intermolecular interaction energy between two adjacent molecules were obtained at the M06-2X/6-31++G(d,p) level of DFT with counterpoise correction for the basis set superposition error. The calculations were performed using the Gaussian 09 program package (Figure S17).

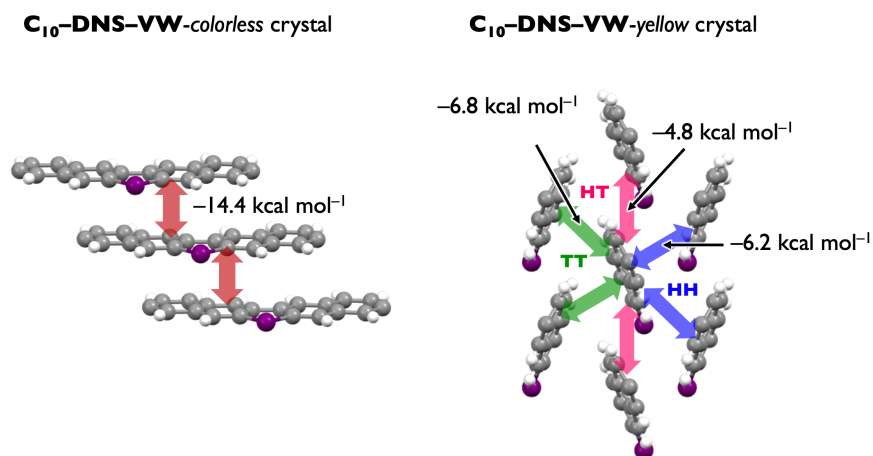


Figure S17. Intermolecular interaction energy of C₁₀-DNS-VW-*colorless* and C₁₀-DNS-VW-*yellow* between two adjacent molecules.

9.4 Transfer Integrals and Band Structure Calculations

Theoretical calculations of transfer integral and effective mass were conducted using the GAMESS package.⁶ The Kohn–Sham eigenstates of all of compounds in this work were calculated at the PBEPBE/6-31G(d) level of theory. Based on their packing structures, the transfer integrals (t) of HOMO–HOMO and NHOMO–NHOMO of neighboring molecules were estimated by the dimer method.⁷

To further understand the carrier transporting capabilities in the single-crystal state, their HOMO band structures $E(k)$ were also calculated by the tight-binding approximation using transfer integrals. Effective masses of electron were calculated as $m^* = |\hbar^2(\partial^2 E(k)/\partial k^2)^{-1}|$ along respective directions.

Table S4. Summary of transfer integrals of V-shaped derivatives.

Compounds	Packing mode and HB angles(°)	Transfer integrals, t (meV) ^a					Effective masses	
		t_{HT}	t_{HH}	t_{TT}	t_1	t_2	m_{\parallel}^*/m_0^* , m_{\perp}^*/m_0^*	m_b^*/m_0^* , m_a^*/m_0^{*c}
C₁₀–DNF–VW	HB, 48.1°	–1.4 ^b –17.5 ^c	–2.5 ^b –76.4 ^c	–15.4 ^b –77.8 ^c	–	–	5.2, 1.8	–
C₁₀–DNT–VW	HB, 49.2°	+17.6 ^b +45.2 ^c	–32.4 ^b –36.7 ^c	–13.7 ^b –60.6 ^c	–	–	1.5, 2.7	–
C₁₀–DNS–VW -yellow phase	HB, 46.2°	+60.8 ^b +18.4 ^c	–61.8 ^b –11.9 ^c	–25.0 ^b –20.8 ^c	–	–	1.2, 3.5	–
C₁₀–DNS–VW -colorless phase	1D π -stacking	–	–	–	–96.0 ^b –61.5 ^c	+0.7 ^b +0.7 ^c	–	>6, 1.9

^a Transfer integrals are calculated at the PBEPBE/6-31G(d) level of theory.

^b Transfer integrals between HOMOs.

^c Transfer integrals between NHOMOs.

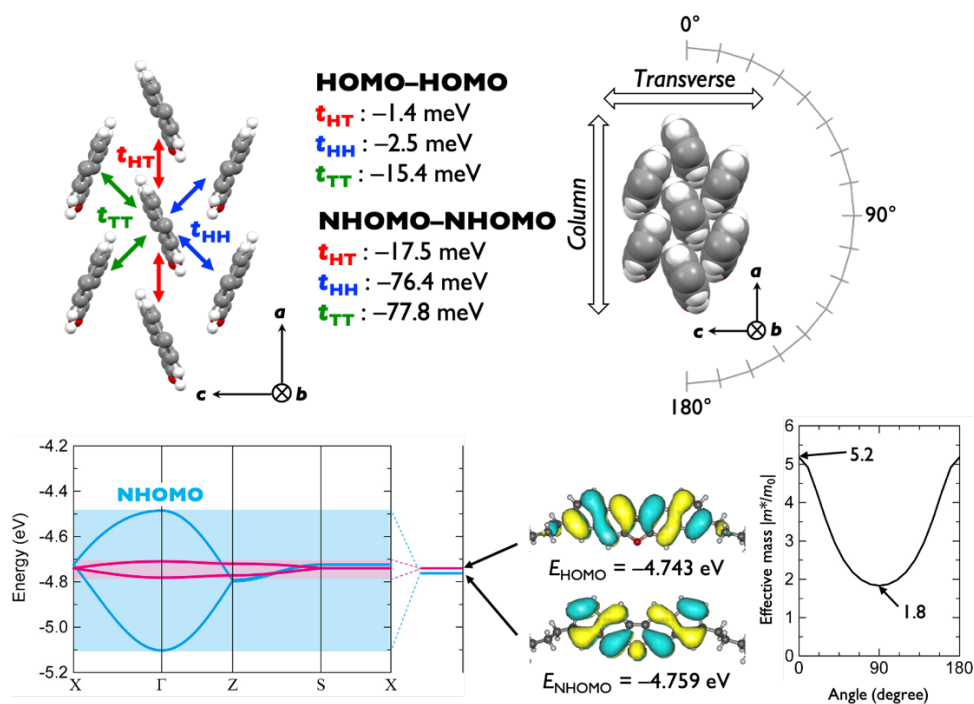


Figure S18. Packing structure of **C₁₀-DNF-VW** along with transfer integrals of HOMO-HOMO and NHOMO-NHOMO, electronic band structure of **C₁₀-DNF-VW** crystal (*a-c* plane) along with E_{HOMO} and E_{NHOMO} , and effective masses of **C₁₀-DNF-VW** crystal (*a-c* plane) depending on angles from column direction (calculated at the PBE/PBE/6-31G(d) level).

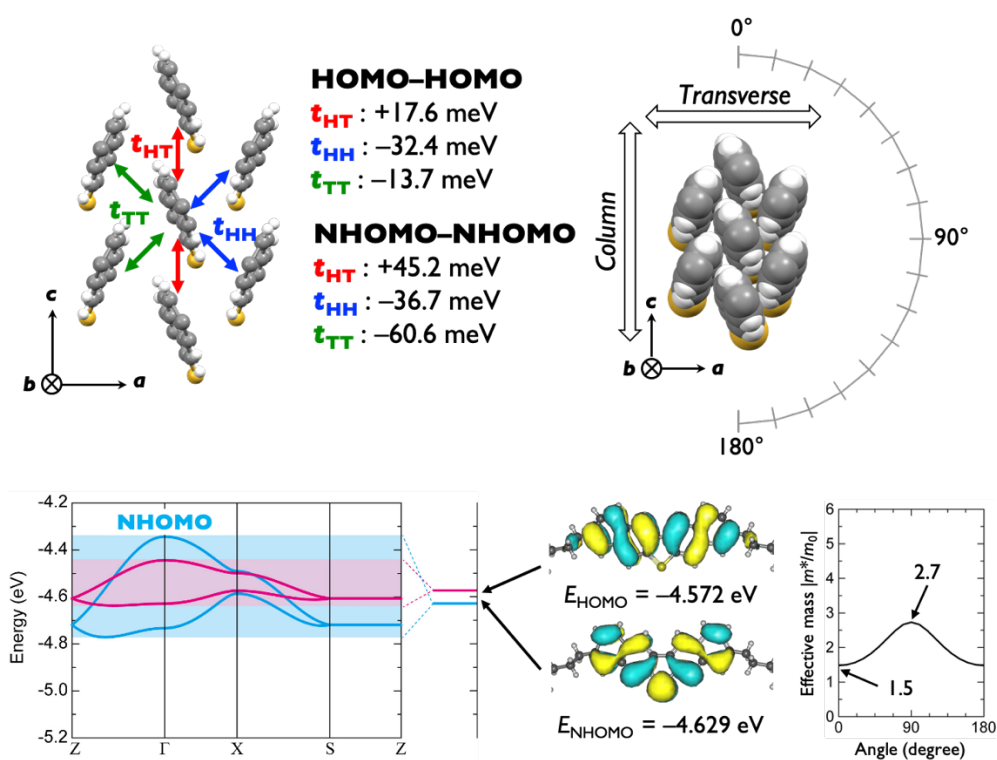


Figure S19. Packing structure of **C₁₀-DNT-VW** along with transfer integrals of HOMO-HOMO and NHOMO-NHOMO, electronic band structure of **C₁₀-DNT-VW** crystal (*a-c* plane) along with E_{HOMO} and E_{NHOMO} , and effective masses of **C₁₀-DNT-VW** crystal (*a-c* plane) depending on angles from column direction (calculated at the PBE/PBE/6-31G(d) level).

10. X-ray Diffraction Measurement and AFM Observation for Polycrystalline Films

To estimate aggregation structures of vapor-deposited **C₁₀–DNS–VW** polycrystalline films, the X-ray-diffraction data of vapor-deposited films were collected using Rigaku Mercury 70 with CuK α (wavelength: 1.54056 Å) radiation. Independent of substrate temperature, the all out-of-plane diffraction patterns give only (0 *k* 0) peaks under assumption that polycrystalline films have the same aggregation structure as a single crystal of **C₁₀–DNS–VW-yellow**, as shown in Figure S20. Lattice constant was evaluated from a plot of $\sin\theta/\lambda$ vs *k* to be 70.71 Å, which is consistent with *c* = 70.15 Å in a single crystal of **C₁₀–DNS–VW-yellow**. This result clearly indicates that the polycrystalline film by vapor deposition show herringbone packing structure proper to carrier transport.

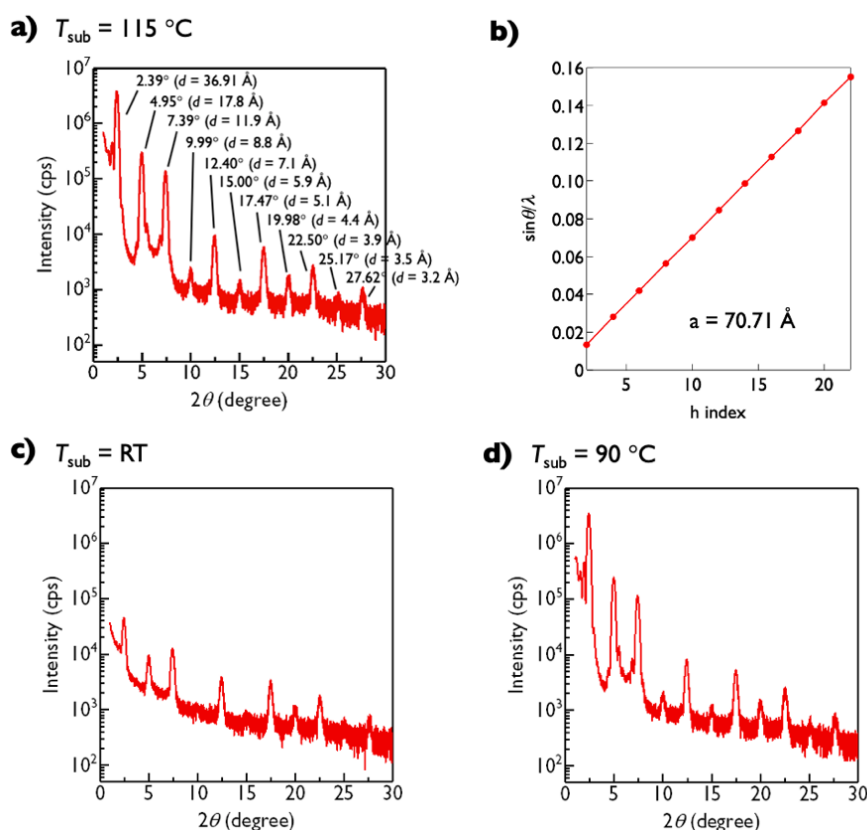


Figure S20. XRD patterns of films deposited at a-b) 115 °C, c) room temperature, and d) 90 °C.

To observe morphology of the polycrystalline films, atomic force microscopy (AFM) images were taken on a Shimadzu SPM 9700-HT with a non-contact mode. The AFM images are shown in Figure S21. As mentioned above, although aggregation structure is not dependent on substrate temperature, morphology is quite dependent on substrate temperature. The film deposited at $T_{\text{sub}} = \text{room temperature}$ has <500-nm small grains, and the films deposited at $T_{\text{sub}} = 90\text{ }^{\circ}\text{C}$ and $115\text{ }^{\circ}\text{C}$ have no obvious grains. Reflected the difference of morphology and grain size, mobility values of the films deposited at room temperature are lower than that of films deposited at $90\text{ }^{\circ}\text{C}$ and $115\text{ }^{\circ}\text{C}$. Moreover, heights of steps are consistent with a molecular long axis of $\text{C}_{10}\text{-DNS-VW}$, which support that the aggregated structures are same as a $\text{C}_{10}\text{-DNS-VW-yellow}$ crystal and b axis is perpendicular to the substrates.

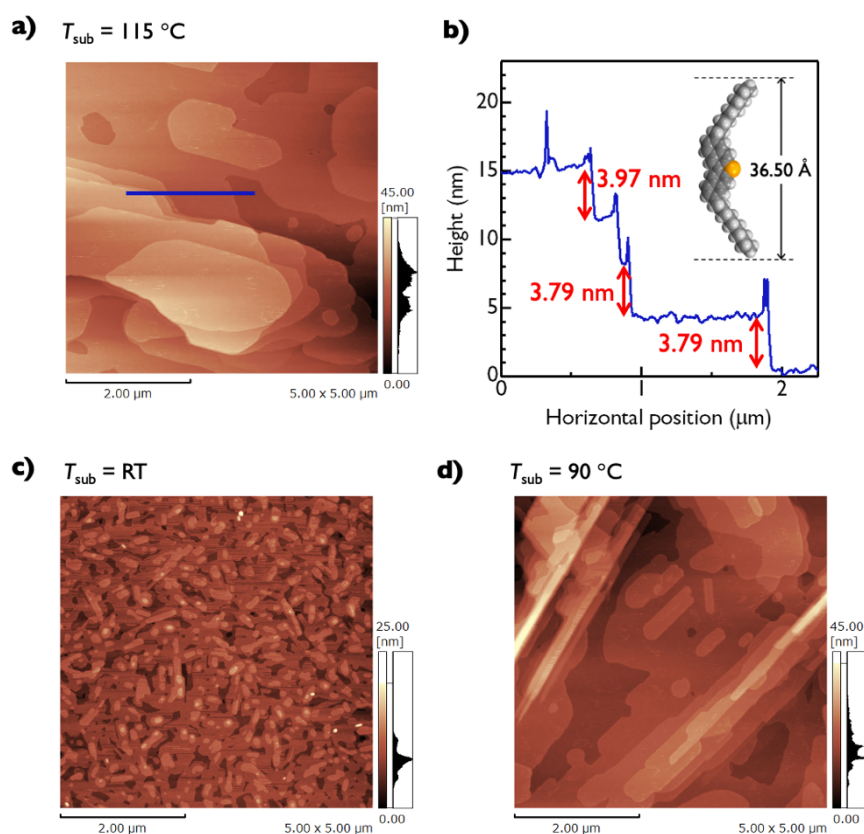


Figure S21. AFM images of films deposited at a) $115\text{ }^{\circ}\text{C}$, c) room temperature, and d) $90\text{ }^{\circ}\text{C}$. b) height profile along blue line in a).

11. OFET Device Fabrication and Evaluation Procedure

11.1 OFET Evaluation

Transfer and output characteristics of organic field-effect transistors (OFETs) obtained were collected using a semiconductor parameter analyzer (Keithley 4200). Field-effect mobility values (μ_{sat}) were estimated from the saturation regime using the following equation:

$$-I_D = (WC_i/2L) \mu_{\text{sat}} (V_G - V_{\text{th}})^2$$

C_i is the capacitance of gate insulator, V_{th} is the threshold voltage, and L and W are length and width of the channel, respectively.

11.2 PVT grown DNS-V single crystal OFET

The surface of the substrates with 500-nm-thick thermally oxidized SiO_2 on doped Si was washed consecutively with acetone and 2-propanol in an ultra-sound bath for each 5 min, followed by the UV ozone treatment. Then, the cleaned substrates were treated with vapor-deposited heptadecafluorodecyltrimethoxysilane (FDTS). A thin single crystal of **DNS-V** grown by PVT (see Section 3 in SI) was electrostatically attached to the FDTS-treated substrate. On top of the laminated single crystals, 2,3,5,6-tetrafluoro-7,7,8,8-tetracyanoquinodimethane ($\text{F}_4\text{-TCNQ}$)⁸⁻⁹ as a strong acceptor (thickness: 2 nm) to reduce contact resistance and gold electrodes (thickness: 30 nm) were successively deposited through the shadow mask to fabricate a bottom-gate-top-contact device. The doped-Si layer acts as a gate electrode and SiO_2 layer as gate dielectrics with relative dielectric constant of 3.9.

DNS-V single crystal transistors operate as p-type OFET with negligible hysteresis. Unfortunately, they show large threshold voltage of approximately -50 V (on 500-nm-thick SiO_2). From transfer characteristics in saturation region, mobility is evaluated to be 0.088 ± 0.013 cm^2/Vs as an average and 0.11 cm^2/Vs as maximum (Figure S22).

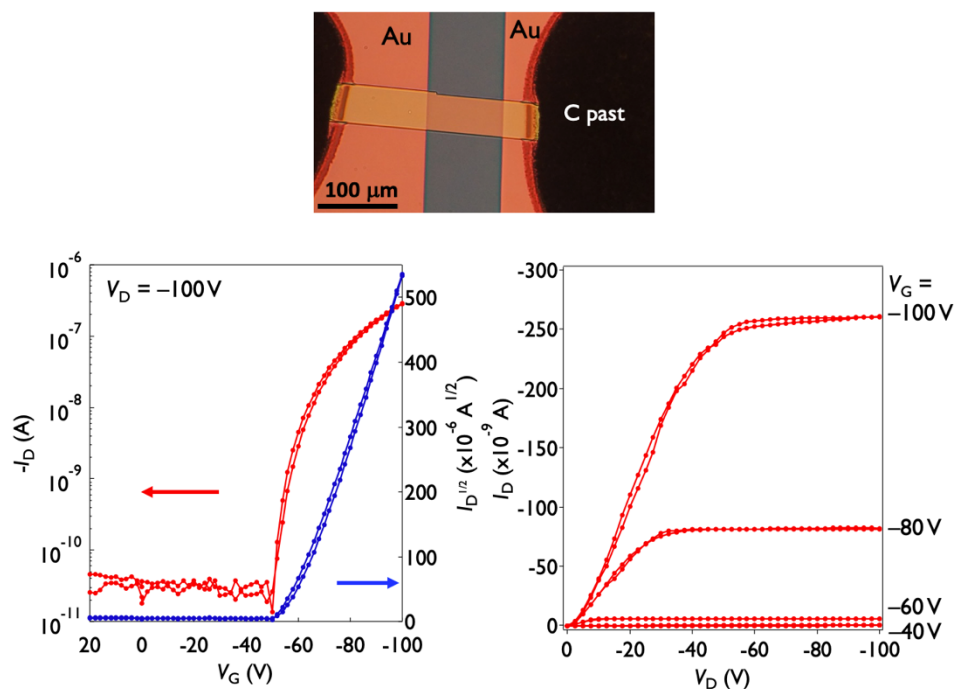


Figure S22. OFET performance of **DNS-V** single crystal. (top) Top view of the device. The carbon past electrically connected Au electrodes on top of the crystal and on the substrate. (bottom-left) Transfer and (-right) output characteristics ($L/W = 100 \mu\text{m}/50 \mu\text{m}$, SiO_2 : 500 nm).

11.3 Vapor-deposited C_{10} -DNS-VW FET

The doped Si substrates with 200-nm-thick SiO_2 , which surface was treated with decyltrimethoxysilane (DTS) vapor, were consecutively washed with acetone and 2-propanol in an ultra-sound bath. Onto the substrates heated at each temperature (T_{sub}), 40-nm-thick films of **C₁₀-DNS-VW** were thermally deposited through shadow masks in a vacuum chamber (rate: 0.5 \AA sec^{-1}). On the top of the polycrystalline films, $\text{F}_4\text{-TCNQ}$ (2 nm)⁸⁻⁹ and gold (60 nm) as contacts were successively deposited through shadow masks to construct bottom-gate-top-contact architectures.

Transfer and output characteristics of the represented device of each substrate temperature are shown in Figure S23–25. All devices operate as p-type OFETs and slight hysteresis against V_G sweeping. Their average mobility values and maximum values are summarized in Table S5. Their mobility becomes higher in order of $T_{\text{sub}} = \text{room temperature}$, 90°C , and 115°C .

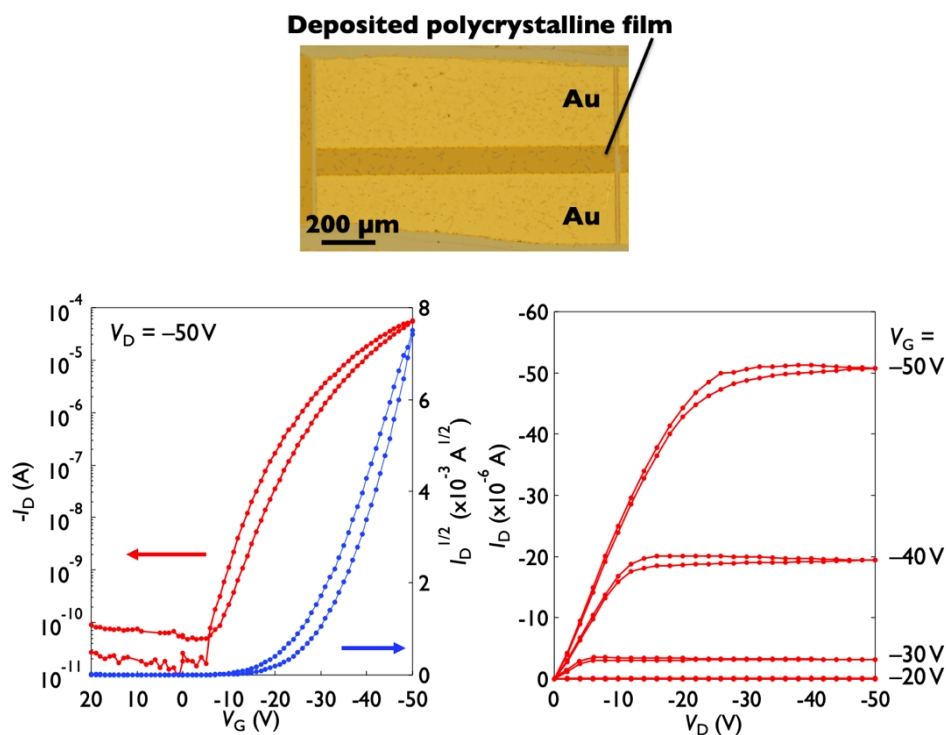


Figure S23. OFET performance of a C_{10} -DNS-VW polycrystalline film deposited at room temperature. (Top) Top view of the device. Transfer (left)- and output (right) characteristics ($L/W = 100 \mu\text{m}/1059 \mu\text{m}$, SiO_2 : 200 nm).

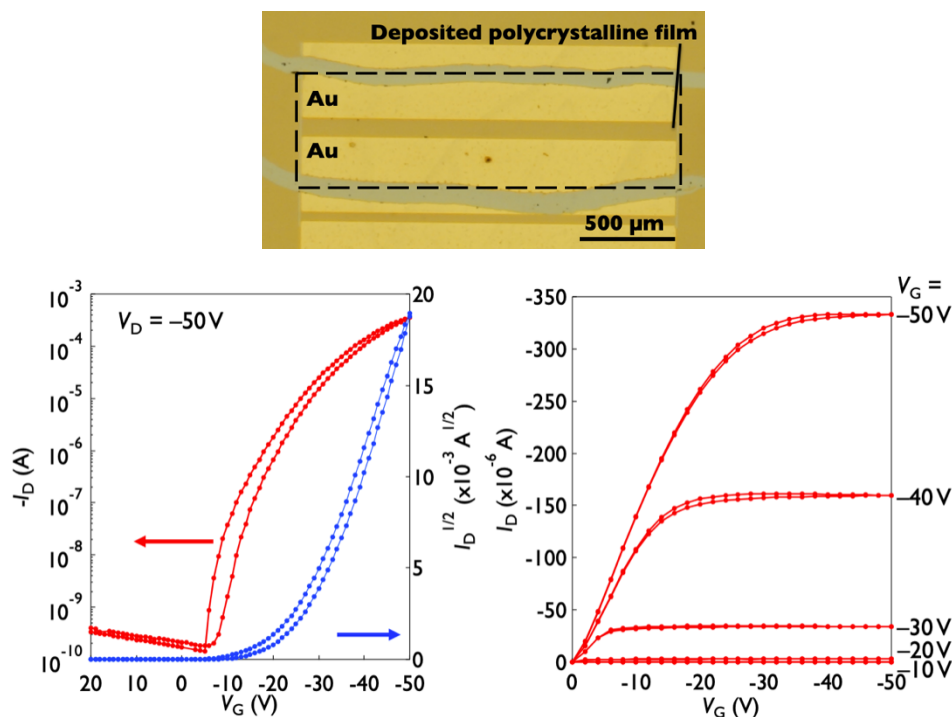


Figure S24. OFET performance of a C_{10} -DNS-VW polycrystalline film deposited at 90 °C.

Transfer (left)- and output (right) characteristics ($L/W = 100 \text{ } \mu\text{m}/2000 \text{ } \mu\text{m}$, SiO_2 : 200 nm).

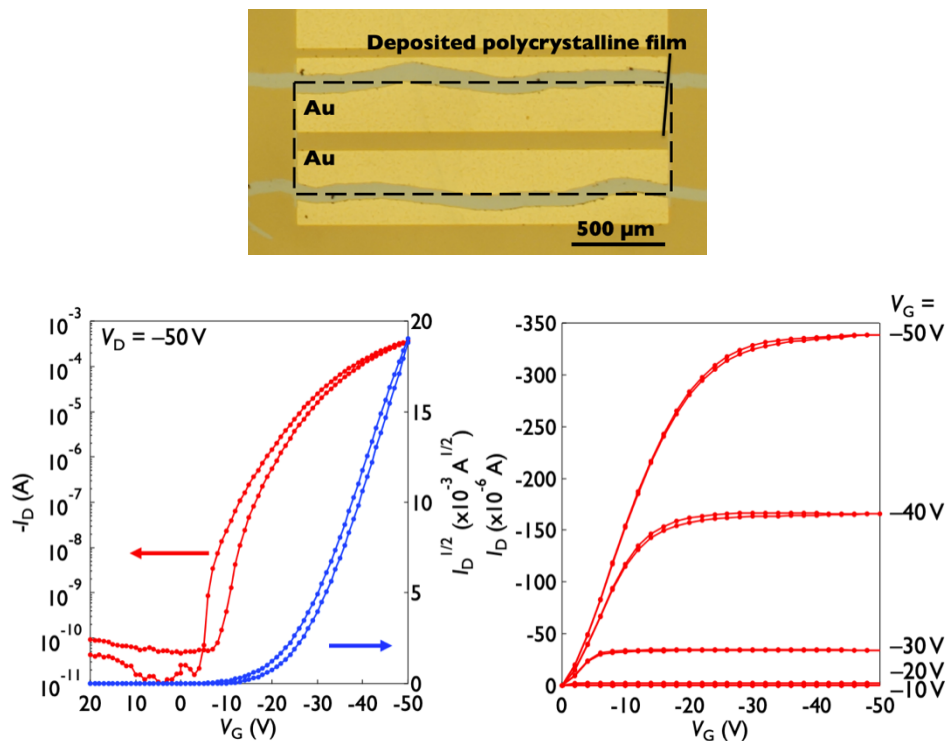


Figure S25. OFET performance of a **C₁₀-DNS-VW** polycrystalline film deposited at 115 °C. (Top) Top view of the device. Transfer (left)- and output (right) characteristics ($L/W = 100 \text{ } \mu\text{m}/2000 \text{ } \mu\text{m}$, SiO_2 : 200 nm).

Table S5. Mobility values of **C₁₀-DNS-VW** polycrystalline films.

T_{sub} (°C)	Mobility (cm^2/Vs)	
	$\mu_{\text{avg}}^{\text{a}}$	μ_{max}
Room temperature	1.0 ± 0.05	1.1
90 °C	2.3 ± 0.6	3.2
115 °C	2.8 ± 0.4	3.2

^a The average mobility is described as an average value along with a standard deviation.

11.4 Solution crystallized C₁₀–DNS–VW-*yellow* FET

The surface of the cleaned 200-nm-thick thermally oxidized SiO₂ on doped Si substrates is treated with β -phenylethyltrimethoxysilane (β -PTS) in toluene solution. To form the crystalline thin films, 0.01 wt% anisole solution of C₁₀–DNS–VW was dropped onto the edge of a sustaining glass piece onto the substrates at 40 °C. The crystalline domains grow in the direction of evaporation of the solvent. After the sustaining pieces were removed, the crystalline films were dried at 70 °C in vacuum for 24 h. Then, F₄–TCNQ (2 nm)⁸⁻⁹ and gold (40 nm) as contacts were evaporated on the C₁₀–DNS–VW film through a shadow mask. Finally, to determine channel size, unnecessary crystals were removed by laser etching technique.

To observe morphology of the solution-crystallized C₁₀–DNS–VW-*yellow* thin-film, AFM images were taken on a Shimadzu SPM 9700-HT with a non-contact mode. The AFM images are shown in Figure S26. As can be seen in Figure S26, it exhibits a smooth surface and a gap of 3.7 nm which corresponds to the molecular length of C₁₀–DNS–VW along the longitudinal axis.

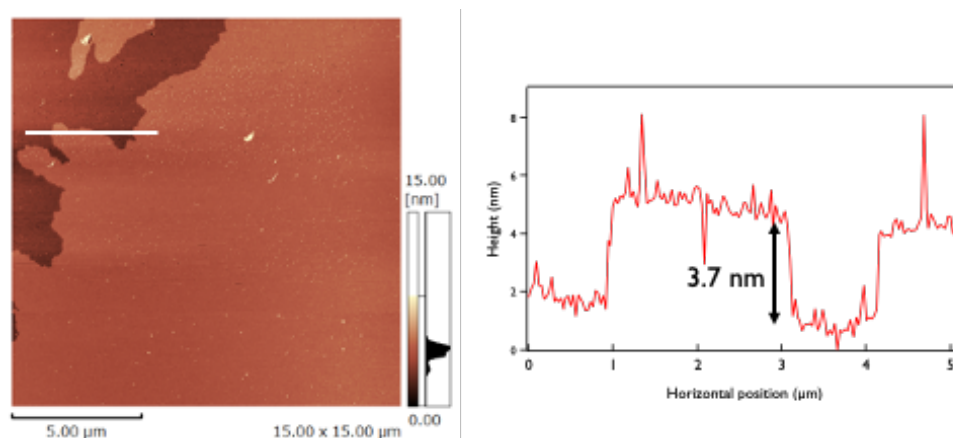


Figure S26. AFM images of the solution-crystallized C₁₀–DNS–VW-*yellow* thin-film.

11.5 Device stability test of solution crystallized C₁₀–DNS–VW–yellow FET against atmospheric stress

The device was stored in a yellow room (light shielded to 500 nm or less) at room temperature in the air. Figure S27 shows the output characteristics of a C₁₀–DNS–VW–yellow solution-grown single-crystal FET over two months.

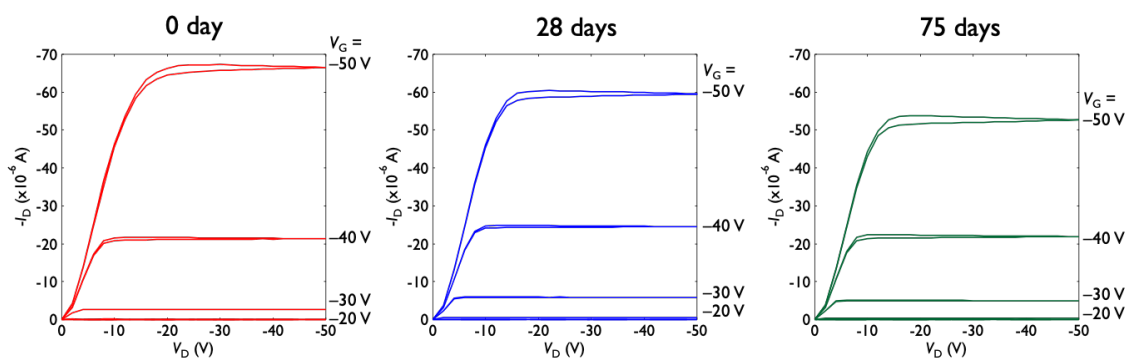


Figure S27. The output characteristics on storage under ambient conditions of a C₁₀–DNS–VW solution-grown single-crystal FET.

11.6 Single crystal FETs with C₁₀–DNS–VW–colorless

To determine the aggregated structures in thin-films, a 100 nm thin-film of C₁₀–DNS–VW–yellow is grown by vapor deposition and then it is exposed to chloroform vapor. Microscope images are summarized in Figure S28. As can be seen from the image after the treatment, needle-like crystals rather than thin films grew on the substrate. Figure S29 shows the result of XRD data to confirm whether the needle-like crystals after the treatment. The XRD before the exposure showed good agreement with the powder pattern of the C₁₀–DNS–VW–yellow form, while the molecules were selectively oriented in the *b*-axis direction on the substrate. On the other hand, the needle-like single crystal grown on the substrate after the vapor treatment showed a good agreement with the powder pattern of the C₁₀–DNS–VW–colorless form and also the yellow form is well converted to the colorless one as shown in Figure S29.

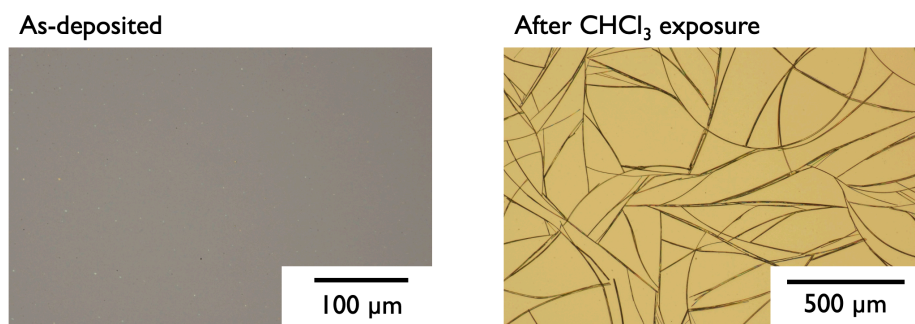


Figure S28. Optical microscope image of vapor-deposited C_{10} -DNS-VW thin film before (as-deposited) and after exposure to $CHCl_3$.

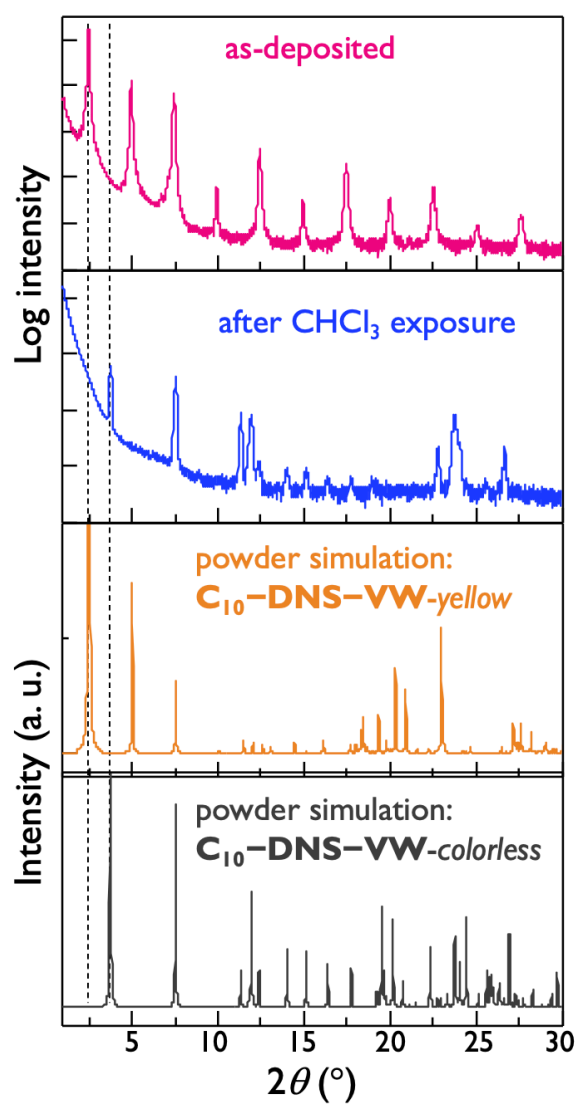


Figure S29. Thin-film XRD patterns of before and after Optical microscope image of

vapor-deposited **C₁₀–DNS–VW** thin film before (as-deposited) and after exposure to CHCl₃ along with powder simulation of **C₁₀–DNS–VW-yellow** and **C₁₀–DNS–VW-colorless** crystal structures.

To prepare well-ordered single-crystals of **C₁₀–DNS–VW-colorless**, **C₁₀–DNS–VW-yellow** crystalline films were fabricated by edge casting method. The dried crystalline film and chloroform were sealed in a glass container at room temperature to expose the film to chloroform vapor overnight. The exposure changed the crystalline thin film (**C₁₀–DNS–VW-yellow**) into needle crystals (**C₁₀–DNS–VW-colorless**). Onto the needle crystals, F₄–TCNQ (2 nm)⁸⁻⁹ and gold (70 nm) as contacts were deposited through a shadow mask to construct contacts and a bottom-gate-top-contact transistor. Finally, to determine channel size, unnecessary crystals were removed by laser etching technique.

The transfer characteristics for a representative FET with **C₁₀–DNS–VW-colorless** needle crystals were shown in Figure S30. The needle crystals work as p-type organic semiconductors, but they show significant hysteresis against V_G sweep and large threshold voltage, which imply that the 1D-needle crystals are not suitable for carrier transport. Furthermore, the transistor performance was affected by bias stress and output characteristics could not be successfully collected. Actually, their mobility is lower than **C₁₀–DNS–VW-yellow** by 4–5 orders of magnitude (in order of 10^{-4} cm²/Vs). The trend of carrier transport property agrees with calculation results.

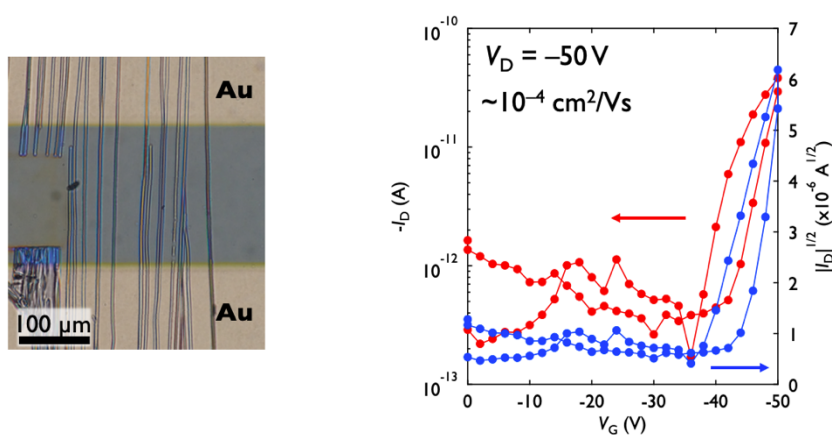


Figure S30. (left) Top view and (right) transfer characteristics of a **C₁₀–DNS–VW-colorless** single crystal transistor.

12. References

- (1) Kondo, Y.; Shilai, M.; Uchiyama, M.; Sakamoto, T. TMP–Zincate as Highly Chemoselective Base for Directed Ortho Metalation. *J. Am. Chem. Soc.* **1999**, *121*, 3539-3540.
- (2) Uchiyama, M.; Miyoshi, T.; Kajihara, Y.; Sakamoto, T.; Otani, Y.; Ohwada, T.; Kondo, Y. Generation of Functionalized Asymmetric Benzyne with TMP-Zincates. Effects of Ligands on Selectivity and Reactivity of Zincates. *J. Am. Chem. Soc.* **2002**, *124*, 8514-8515.
- (3) Uchiyama, M.; Kobayashi, Y.; Furuyama, T.; Nakamura, S.; Kajihara, Y.; Miyoshi, T.; Sakamoto, T.; Kondo, Y.; Morokuma, K. Generation and Suppression of 3-/4-Functionalized Benzyne Using Zinc Ate Base (TMP–Zn–ate): New Approaches to Multisubstituted Benzenes. *J. Am. Chem. Soc.* **2008**, *130*, 472-480.
- (4) Maaninen, A.; Chivers, T.; Parvez, M.; Pietikäinen, J.; Laitinen, R. S. Syntheses of THF Solutions of SeX₂ (X = Cl, Br) and a New Route to Selenium Sulfides SenS₈-n (n = 1–5): X-ray Crystal Structures of SeCl₂(tht)₂ and SeCl₂·tmtu. *Inorg. Chem.* **1999**, *38*, 4093-4097.
- (5) Kato, K.; Hirose, R.; Takemoto, M.; Ha, S.; Kim, J.; Higuchi, M.; Matsuda, R.; Kitagawa, S.; Takata, M. The RIKEN Materials Science Beamline at SPring-8: Towards Visualization of Electrostatic Interaction. *AIP Conference Proceedings* **2010**, *1234*, 875-878.
- (6) Schmidt, M. W.; Baldrige, K. K.; Boatz, J. A.; Elbert, S. T.; Gordon, M. S.; Jensen, J. H.; Koseki, S.; Matsunaga, N.; Nguyen, K. A.; Su, S.; Windus, T. L.; Dupuis, M.; Montgomery Jr, J. A. General atomic and molecular electronic structure system. *J. Comput. Chem.* **1993**, *14*, 1347-1363.
- (7) Valeev, E. F.; Coropceanu, V.; da Silva Filho, D. A.; Salman, S.; Brédas, J.-L. Effect of Electronic Polarization on Charge-Transport Parameters in Molecular Organic Semiconductors. *J. Am. Chem. Soc.* **2006**, *128*, 9882-9886.
- (8) Minari, T.; Miyadera, T.; Tsukagoshi, K.; Aoyagi, Y.; Ito, H. Charge injection process in organic field-effect transistors. *Appl. Phys. Lett.* **2007**, *91*, 053508.
- (9) Mitsui, C.; Okamoto, T.; Yamagishi, M.; Tsurumi, J.; Yoshimoto, K.; Nakahara, K.; Soeda, J.; Hirose, Y.; Sato, H.; Yamano, A.; Uemura, T.; Takeya, J. High-Performance Solution-Processable N-Shaped Organic Semiconducting Materials with Stabilized Crystal Phase. *Adv. Mater.* **2014**, *26*, 4546-4551.